

Experimental n -Hexane-Air Expanding Spherical Flames

Stephanie A. Coronel^{a,*}, Simon Lapointe^{a,**}, Rémy Mével^{b,c}, Vaughan L. Thomas^d,
Nabiha Chaumeix^e, Joseph E. Shepherd^a

^a*Graduate Aerospace Laboratories, California Institute of Technology, Pasadena, California
91125, USA*

^b*Center for Combustion Energy, ^cDepartment of Automotive Engineering, Tsinghua University,
Beijing, China*

^d*Department of Mechanical Engineering, Johns Hopkins University, Baltimore, Maryland 21218,
USA*

^e*ICARE, CNRS-INSIS, 1C Avenue de la Recherche Scientifique, 45071 Orléans Cedex 2, France*

Abstract

The effects of initial pressure and temperature on the laminar burning speed of n -hexane-air mixtures were investigated experimentally and numerically. The spherically expanding flame technique with a nonlinear extrapolation procedure was employed to measure the laminar burning speed at atmospheric and sub-atmospheric pressures and at nominal temperatures ranging from 296 to 422 K. The results indicated that the laminar burning speed increases as pressure decreases and as temperature increases. The predictions of three reaction models taken from the literature were compared with the experimental results from the present study and previous data for n -hexane-air mixtures. Based on a quantitative analysis of the model performances, it was found that the most appropriate model to use for predicting laminar flame properties of n -hexane-air mixtures is JetSurF.

Keywords: Nonlinear fitting, Laminar burning speed, Markstein length, Spherical flame

*Corresponding author: scorone@sandia.gov; current address: Sandia National Laboratories, Albuquerque, NM

**Current address: Lawrence Livermore National Laboratories, Livermore, CA

1. Introduction

During aircraft operation, the pressure within the fuel tank and other areas potentially containing flammable mixtures varies between 20 and 100 kPa. To assess the risk of potential ignition hazards and flammability in fuel tank ullage or flammable leakage zones, it is necessary to characterize properties such as the laminar burning rate of fuel-air mixtures over a wide range of initial pressures and temperatures. *n*-Hexane has been extensively used at the Explosion Dynamics Laboratory as a single component surrogate of kerosene [1, 2, 3, 4]; *n*-hexane exhibits a relatively high vapor pressure which facilitates experimenting at ambient temperature. In contrast to *n*-heptane, which has been widely studied, *n*-hexane oxidation has received little interest [5]. Curran et al. [6] studied hexane isomer chemistry through the measurement and modeling of exhaust gases from an engine. The ignition delay-time behind a shock wave was measured by Burcat et al. [7], Zhukov et al. [8], Zhang et al. [9], Mével et al. [10]. Zhang et al. [9] also measured the ignition delay-time in the low-temperature regime using a rapid compression machine as well as species profiles using the jet-stirred reactor technique. Mével et al. [11] employed a flow reactor along with gas chromatography (GC) analyses and laser-based diagnostics to measure the species profiles in the temperature range 600 – 1000 K. Boettcher et al. [1] studied the effect of the heating rate on the low temperature oxidation of *n*-hexane by air, and the minimum temperature of a heated surface required to ignite *n*-hexane-air mixtures [4]. Bane [2] measured the minimum ignition energy of several *n*-hexane-air mixtures. A limited number of studies have been found on the laminar burning speed. Davis and Law [12] measured the laminar burning speed of *n*-hexane-air mixtures at ambient conditions using the counterflow twin flame technique. Farrell et al. [13] used pressure traces from spherically expanding flames to determine the laminar burning speed of *n*-hexane-air mixtures at an initial temperature and pressure of 450 K and 304 kPa, respectively. Kelley et al. [14] reported experimental measurements using spherically expanding flames at an initial temperature of 353 K and an initial pressure range of 100 – 1000 kPa. Ji et al. [15] used the counterflow burner technique to measure the laminar burning speed of *n*-hexane-air mixtures at an initial temperature and pressure of 353 K and

100 kPa, respectively.

In contrast to previous work, the present study focuses on initial conditions below atmospheric pressure in order to simulate aircraft fuel tank conditions. Additionally, this study investigates the effect of initial temperature at sub-atmospheric conditions to simulate elevated temperature conditions in the fuel tank ullage or flammable leakage zones.

2. Experimental Setup and Methodology

2.1. Facilities

Two experimental facilities were used in the present study to cover a wide range of initial temperature conditions: the Explosion Dynamics Laboratory (EDL) at the California Institute of Technology (Caltech) and the Institut de Combustion Aérothermique Réactivité et Environnement (ICARE)-Centre National de la Recherche Scientifique (CNRS) Orléans. At the EDL, the experiments were performed in a 22 L stainless steel combustion vessel. Parallel flanges were used to mount electrodes for the ignition system and windows for optical access. The mixtures were ignited by a 300 mJ electric spark generated between two 0.4 mm in diameter tungsten electrodes separated by a distance of 2 – 4 mm. A high-speed camera (Phantom v711) was used to record the flame propagation observed using Schlieren visualization and shadowgraphy at a rate of 10,000 frames per second with a resolution of 512×512 px. The experiments conducted at ICARE-CNRS were performed in a stainless steel spherical bomb consisting of two concentric spheres; the internal sphere had an inner diameter of 476 mm. The mixtures were ignited by electric sparks with a nominal energy of 1.82 mJ. Schlieren visualization was used with a high-speed camera (Phantom V1610) at a rate of 25,000 frames per second with a resolution of 768×768 px.

2.2. Flame Edge Detection

The flame radius as a function of time was extracted from the experimental images of expanding spherical flames using algorithms implemented in Matlab, including an edge detection operator [16, 17]. The images of the spherically propagat-

ing flames were processed by first applying a mask over each image to remove the background (electrodes). Edge detection was then used to identify the expanding flame edge. An ellipse was fitted to the detected flame edge; the ellipse parameters were then used to obtain an equivalent radius. For the majority of the experimental images, the flame sphericity was approximately equal to 1.

2.3. Extrapolation of Flame Parameters

Using asymptotic methods based on large activation energy, Ronney and Sivashinsky [18] obtained a nonlinear model for spherical flame speed as a function of curvature (Eq. 1).

$$\left(\frac{S_b}{S_b^0}\right)^2 \ln\left(\frac{S_b}{S_b^0}\right) = -2\frac{L_B\kappa}{S_b^0}. \quad (1)$$

S_b and S_b^0 are the stretched and unstretched flame speeds, respectively, L_B is the burnt gas Markstein length, and κ is the stretch rate. Karlovitz et al. [19] expressed the stretch rate in terms of the normalized rate of change of an elementary flame front area as,

$$\kappa = \frac{1}{A} \frac{dA}{dt}, \quad (2)$$

where A is the flame front area. In the case of a spherical flame, the flame surface is given by $A = 4\pi R_f^2$, leading to the following expression for the stretch rate [20, 21, 22, 23]:

$$\kappa = 2\frac{S_b}{R_f}, \quad (3)$$

and given that the flame speed corresponds to the flame radius increase rate,

$$S_b = \frac{dR_f}{dt}. \quad (4)$$

The measured rate of increase of the flame radius, dR_f/dt , is assumed to be the flame speed since the combustion products are stationary in the laboratory frame. In the case of a large volume vessel and for measurements limited to the initial period of propagation when the flame radius is small compared to the experimental set-up dimensions, the pressure increase can be neglected [24].

Combining Eqs. 3 and 1 and simplifying the logarithmic term leads to the following relation,

$$\frac{S_b}{S_b^0} \ln\left(\frac{S_b}{S_b^0}\right) = -2\frac{L_B}{R_f}. \quad (5)$$

Since the flame speed is positive, the term on the left hand side may take on values only within the range $[-e^{-1}, \infty)$. For $L_B < 0$ a solution exists for all positive values of R_f , but for $L_B > 0$, a solution exists only if ,

$$\frac{R_f}{2L_B} \geq e \quad (L_B > 0). \quad (6)$$

Thus for positive Markstein lengths, there exists a minimum flame radius below which the quasi-steady relationship between flame speed and stretch rate is not valid, and hence the unstretched flame speed cannot be extracted using Eqs. 1 or 5. This constraint can be viewed as a maximum Markstein length, $L_{B,\max}$, for a fixed minimum (or initial) flame radius. The fact that no solutions exist for small flame radii is a consequence of the neglected unsteady term which is important in the early-time flame dynamics [18]. This limitation was also identified by Lipatnikov et al. [25].

Equation 5 is used to derive the unstretched flame speed and the Markstein length from experimental data. One approach to doing this is to analyze the flame radius history $R_f = f(t)$ data applying polynomial fits and differentiating to determine $S_b = dR_f/dt$ [26, 27]. Numerical differentiation of the experimental data leads to amplification of existing noise. To avoid differentiating the experimental data, Kelley and Law [28] proposed an integrated form of Eq. 1. In the present study, numerical integration rather than analytic integration is used to extract the flame properties from the nonlinear result of Ronney and Sivashinsky [18]. The unstretched burning speed, S_u^0 is obtained through $S_u^0 = S_b^0/\sigma$, where σ is the expansion ratio defined as $\sigma = \rho_u/\rho_b$, where ρ_u and ρ_b are the unburnt and burnt gas densities, respectively. For the remainder of this study, the unstretched burning speed will be referred to as the laminar burning speed.

3. Results and Discussion

3.1. Experimental Results

Experimental laminar burning speeds at an initial temperature of 296 K and pressure of 100 kPa are shown in Fig. 1 along with results previously obtained by Davis and Law [12]. The uncertainty in the laminar burning speeds is on average

6%, the value is based on previous estimates made by Mével et al. [17] who used the same flame detection algorithms employed in the present study. Figure 1 also shows 1D freely propagating flame calculations performed using FlameMaster [29] with three different chemical kinetic mechanisms: CaltechMech [30], JetSurF [31], and the mechanism of Mével et al. [11] (referred to as Mével in this study). Further details on mechanism description and performance are provided in Section 3.2. A Mann-Whitney-Wilcoxon (MWW) RankSum test indicated that the differences in the two laminar burning speed distributions shown in Fig. 1 were not statistically significant; details of the test can be found in the Appendix.

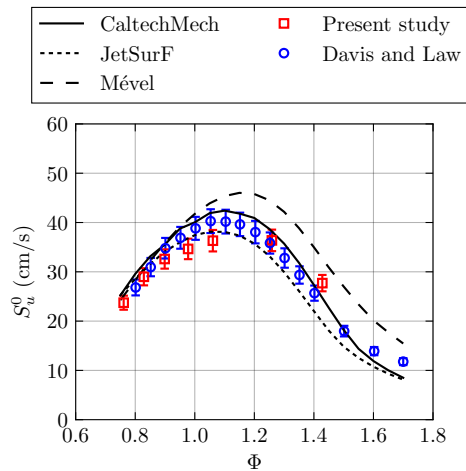


Figure 1: Experimental laminar burning speed of *n*-hexane-air mixtures as a function of equivalence ratio at a nominal initial temperature and pressure of 300 K and 100 kPa, respectively, along with numerical calculations (CaltechMech [30], JetSurF [31], and Mével [11]).

The evolution of the laminar burning speed as a function of equivalence ratio was studied at a nominal initial temperature and pressure of 300 K and 50 kPa, respectively. Figure 2 shows the laminar burning speed obtained at initial pressures of 100 kPa and 50 kPa. The MWW RankSum test indicated that the differences in the laminar burning speed distributions at 100 kPa and 50 kPa were not statistically significant.

The effect of initial pressure on the laminar burning speed was investigated at $\Phi = 0.90$ and a nominal initial temperature of 357 K. The experimental laminar burning speed is shown in Fig. 3 along with experimental results obtained by Kelley

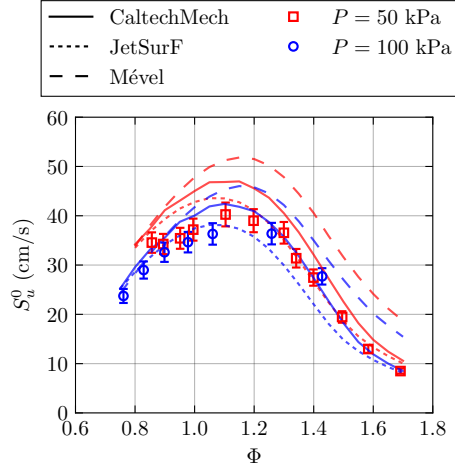


Figure 2: Experimental laminar burning speed of *n*-hexane-air mixtures as a function of equivalence ratio at nominal initial pressures of 50 kPa and 100 kPa and nominal initial temperature of 300 K; numerical calculations (CaltechMech [30], JetSurF [31], and Mével [11]) also shown.

et al. [14] at initial pressures of 100 – 1000 kPa and an initial temperature of 353 K. The laminar burning speed decreases with increasing initial pressure, 20% between 50 and 100 kPa and 53% between 50 and 1000 kPa at nominal initial temperatures of 353 and 357 K. The pressure dependence on the laminar burning speed can be fit to a power law: $S_u^0(P) = 128 \times P^{-0.24}$, where P has units of kPa. The corresponding standard deviations for the pre-exponential and exponent are 12 and 0.02, respectively.

The effect of initial temperature was studied at an initial pressure of 50 kPa and three equivalence ratios, $\Phi = \{0.90, 1.10, 1.40\}$. The laminar burning speed and flux are shown in Fig. 4. At initial temperatures of 296 K to 422 K, the laminar burning speed increases by approximately 93%, 82%, and 94% for $\Phi = 0.90$, $\Phi = 1.10$, and $\Phi = 1.40$, respectively. There is a distinct difference between the laminar burning speeds distributions shown for $\Phi = \{0.90, 1.10, 1.40\}$. Each distribution can be fit to a power law $S_u^0 \sim T^2$ shown in Fig. 4; however, the best fit for each distribution is $S_u^0 \sim T^{1.9}$ ($\Phi = 0.90$), $S_u^0 \sim T^{1.7}$ ($\Phi = 1.10$), and $S_u^0 \sim T^{1.9}$ ($\Phi = 1.40$). The standard deviation of the exponents in the best fits is 0.1.

Figure 5 shows the variation of the Markstein length with equivalence ratio at an initial temperature and pressure of 296 K and 50 kPa, respectively. Lean and

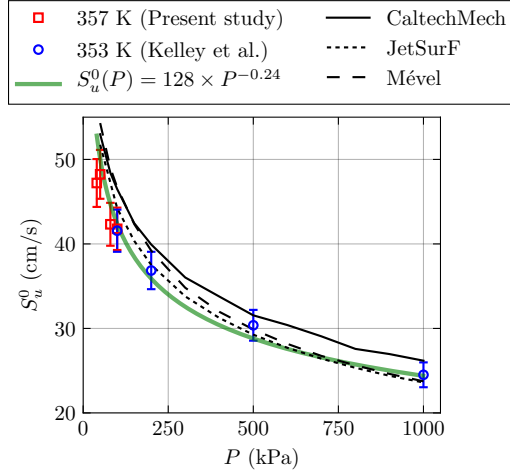


Figure 3: Experimental laminar burning speed of *n*-hexane-air mixtures as a function of initial pressure at an initial temperature of 353 and 357 K along with numerical calculations (CaltechMech [30], JetSurF [31], and Mével [11]).

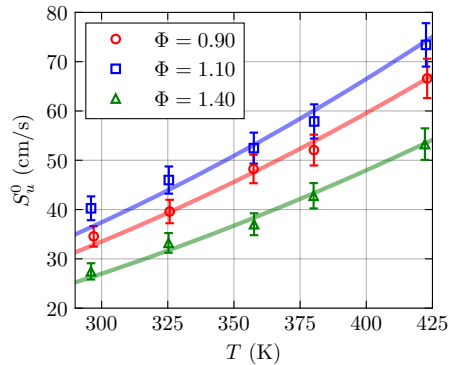


Figure 4: Experimental laminar burning speed of *n*-hexane-air mixtures as a function of initial temperature at an initial pressure of 50 kPa and $\Phi = 0.9, 1.1, \text{ and } 1.4$; the solid lines correspond to $S_u^0 \sim T^2$.

rich mixtures exhibit positive and negative Markstein lengths, respectively. The transition from positive to negative Markstein length occurs at $\Phi \approx 1.3$. This trend is consistent with previous Markstein length results obtained for C_5 to C_8 *n*-alkane-air mixtures [14]. Figure 5 shows the Markstein length extrapolated using a linear and nonlinear dependence of the stretched flame speed on stretch rate. The linear dependence on stretch rate is given by $S_b = S_b^0 - L_B \kappa$. It is evident from the figure that deviations of the nonlinear L_B from the linear L_B occur for both rich and lean

n-hexane-air mixtures.

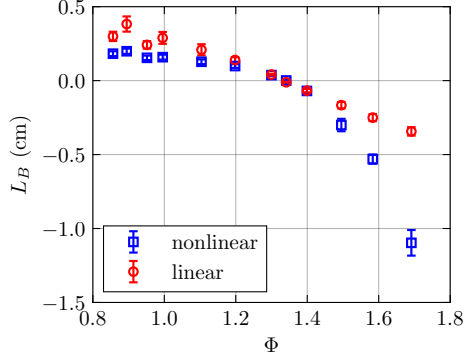


Figure 5: Evolution of the Markstein length for *n*-hexane-air mixtures as a function of equivalence ratio at a nominal initial temperature and pressure of 296 K and 50 kPa, respectively, using linear and nonlinear extrapolations.

The radii range and number of points used to extract the Markstein lengths of Fig. 5 are shown in Table 1 where N is the number of flame radius points, and R_{f_0} and R_{f_N} are the initial and final flame radius. The values of R_{f_N} across all tests is between 40 and 50 cm; Huo et al. [32] indicated that a final flame radius of 40 cm compared to 20 cm reduced the error in extrapolation of the flame parameters from 6% to 3% and 8% to 4% for H_2 -air at $\Phi = 4.5$ and C_3H_8 -air at $\Phi = 0.8$, respectively.

Figure 6 shows the product of the Markstein number, Ma_{linear} (obtained via the linear extrapolation method), and the Karlovitz number, Ka_{mid} (evaluated at the mid-point of the flame radii data), as a function of the mixture equivalence ratio. The product is suggested by Wu et al. [33] as a method to evaluate the uncertainty of the extrapolation method. In Fig. 6, the blue, green, and red regions have extrapolation uncertainties of $\leq 5\%$, 5 – 12%, and 5 – 40%, respectively. The points lying in the red region correspond to rich conditions at a nominal initial temperature and pressure of 296 K and 50 kPa, respectively.

Figure 7 shows examples of a stable lean mixture and an unstable rich mixture flame propagation. For the lean mixture shown in Fig. 7 (a), the flame front remains smooth and undisturbed during the propagation within the field of view $R_f \leq R_{\text{window}}$, where R_{window} is the window radius. For the rich mixture shown in

Test	Φ	N	Range (mm)	R_{f_0} (mm)	R_{f_N} (mm)
24	0.85	147	32	14	46
44	0.86	139	30	14	44
20	0.89	168	34	12	46
40	0.90	159	36	11	47
43	0.95	119	31	14	45
26	0.99	160	37	10	47
18	1.00	149	39	9	48
27	1.10	129	36	9	47
39	1.11	124	37	10	47
29	1.20	128	37	9	46
30	1.20	123	36	10	46
9	1.30	116	36	8	44
31	1.30	139	37	10	47
41	1.34	140	35	10	45
32	1.40	155	35	10	45
33	1.50	193	35	10	45
34	1.58	166	20	25	45
42	1.69	219	22	19	41

Table 1: Properties of experimental flame radius distributions used in obtaining Markstein lengths shown in Fig. 5.

Fig. 7 (b), the flame front becomes progressively more disturbed as it grows, and exhibits significant cellular structures before the flame exits the field of view. The development of the cellular pattern is likely due to thermo-diffusive instabilities that are characteristic of rich hydrocarbon-air mixtures [34]. These instabilities create a flame that is no longer spherical and therefore the flame radius measurements are no longer correct because of the unknown relationship between the average flame radius and the flame surface.

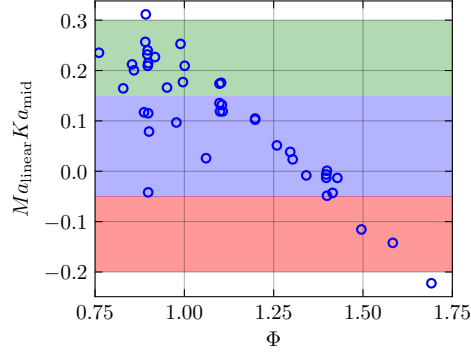


Figure 6: $Ma_{\text{linear}}Ka_{\text{mid}}$ as a function of equivalence ratio for initial temperatures and pressures of 296 K to 380 K, and 40 kPa to 100 kPa, respectively.

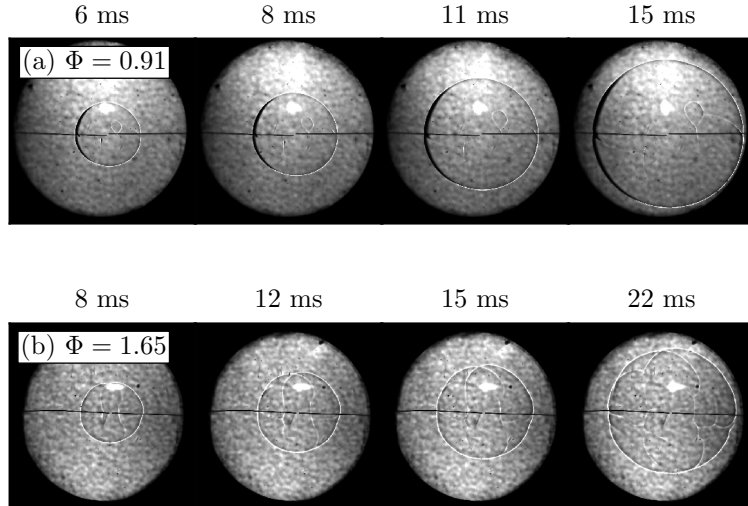


Figure 7: Example of (a) stable and (b) unstable flame propagation of *n*-hexane-air mixtures at an initial temperature and initial pressure of 296 K and 50 kPa, respectively.

3.2. Modeling Results

The 1D freely propagating flame calculations performed with FlameMaster [29] used the chemical kinetic mechanisms of CaltechMech [30], JetSurF [31], and Mével [11]. The calculations neglected Soret and Dufour effects, and a mixture-averaged formulation was used for the transport properties. Ji et al. [15] showed that using a multicomponent transport coefficient formulation rather than mixture-averaged transport properties resulted in a 1 cm/s increase in the calculated laminar burning speeds of C₅-C₁₂ *n*-alkane mixtures. A study by Xin et al. [35] found that accounting

for Soret effects resulted in a maximum of 1 – 2% increase in the laminar burning speed of *n*-heptane-air flames at and near stoichiometric conditions. Finally, Bongers and Goey [36] showed that for C₃ laminar premixed flames, the effect of excluding Dufour effects was negligible.

Blanquart et al. [30] developed CaltechMech for the combustion of engine relevant fuels; the mechanism consists of 172 species and 1,119 reactions. It should be noted that Blanquart et al. [30] placed importance on the accurate modeling of formation of soot precursors for fuel surrogates in premixed and diffusion flames. Blanquart et al. [30] performed extensive validation of CaltechMech using experimental ignition delay time and laminar burning speed data. The flame calculations performed by Blanquart et al. [30] included Soret and Dufour effects, and mixture-averaged transport properties.

Wang et al. [31] developed JetSurF for high temperature applications of *n*-alkanes, along with other fuels (cyclohexane, and methyl-,ethyl-,*n*-propyl and *n*-butyl-cyclohexane). The JetSurF version used in the present study consists of 348 species and 2,163 reactions. Calculations have been performed with previous versions of JetSurF and compared against experimental laminar burning speeds of *n*-alkanes by Davis and Law [12], You et al. [37], Smallbone et al. [38], Ji et al. [15], Kelley et al. [14]. Experimental laminar burning speed measurements used for comparison with JetSurF 1.0 calculations were performed by Ji et al. [15], Kelley et al. [14]; the results are shown in Fig. 8 along with the modeling results obtained in the present study.

Mével et al. [11] developed the last chemical kinetic reaction mechanism, consisting of 531 species and 2,628 reactions, presented in this study. The mechanism was not validated against experimental laminar burning speeds since that was outside the scope of the study presented by Mével et al. [11].

3.2.1. Model Performance

Figures 1 to 4 show comparisons between the experimental and calculated laminar burning speeds. Additional comparisons are shown in Fig. 8 for data from Ji et al. [15] and Kelley et al. [14]. Visual inspection of the figures indicates that the

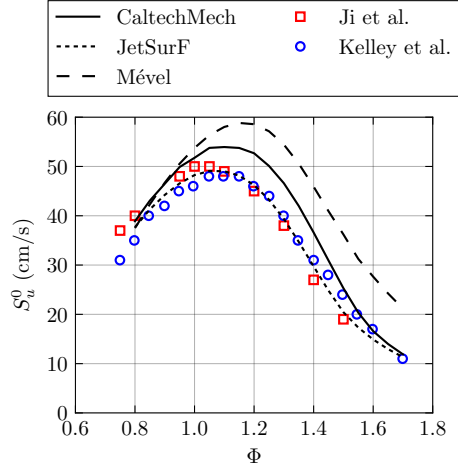


Figure 8: Experimental and numerical (CaltechMech [30], JetSurF [31], and Mével [11]) laminar burning speed of *n*-hexane-air mixtures as a function of equivalence ratio at an initial temperature and pressure of 353 K and 100 kPa, respectively.

chemical kinetic mechanism of Mével cannot predict the laminar burning speed with appropriate accuracy. On the other hand, the predictions of CaltechMech and JetSurF appear to be more accurate; however, it is difficult to ascertain qualitatively which mechanism performs best. The performance of each mechanism is quantitatively evaluated using the root-mean-squared error formulation,

$$\text{RMSE} = \sqrt{\frac{1}{N} \sum_{i=1}^N \left(S_{\text{calc}}^{(i)} - S_{\text{exp}}^{(i)} \right)^2}, \quad (7)$$

where S_{calc} and S_{exp} are the calculated and experimental laminar burning speeds, respectively, N is the number of points for each experimental data set, and i corresponds to the i^{th} point in a data set. The RMSE is calculated for the experimental data sets shown in Table 2. A total of 87 points are used to evaluate the performance of each mechanism, shown in Fig. 10.

Overall, JetSurF yields the smallest RMSE values for almost all the experimental conditions presented in this study and previous studies. The RMSE based on set A ($P = 100$ kPa and $T = 300$ K) is the same between JetSurF (RMSE = 3.5 cm/s) and CaltechMech; the RMSE based on set B (experiments performed by Davis and Law [12]) is smaller, by approximately 19%, for CaltechMech (RMSE = 2.1 cm/s) than JetSurF (RMSE = 2.6 cm/s). For almost all the experimental conditions

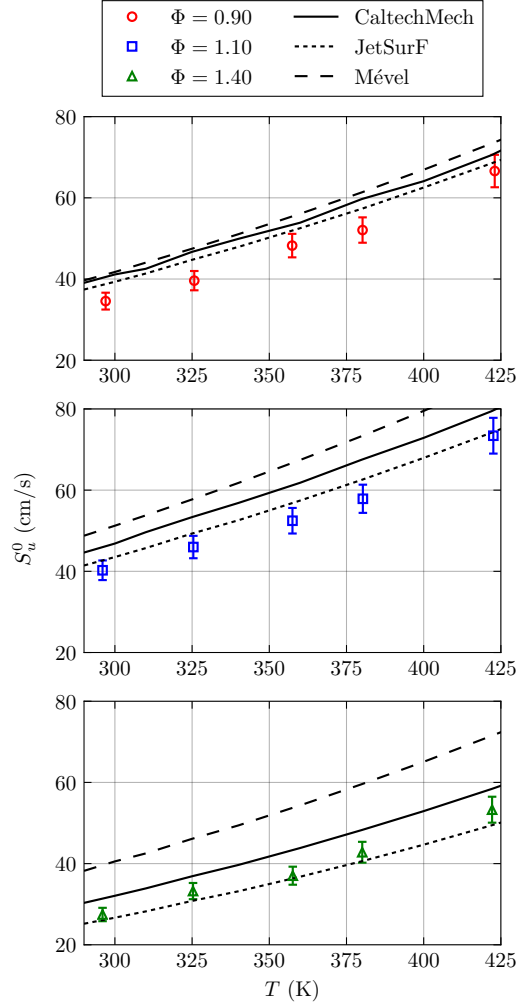


Figure 9: Experimental laminar burning speed of n -hexane-air mixtures as a function of initial temperature at an initial pressure of 50 kPa and $\Phi = 0.9$, 1.1, and 1.4 along with numerical calculations (CaltechMech [30], JetSurF [31], and Mével [11]).

presented, Mével (RMSE = 2.9 – 14.8 cm/s) yields the largest RMSE values when compared to those obtained with JetSurF and CaltechMech. The RMSE based on set J (experiments performed by Kelley et al. [14]) is smaller, by approximately 6%, for Mével (RMSE = 2.9 cm/s) than CaltechMech (RMSE = 3.1 cm/s). When considering the RMSE of sets F, G, and H, ($P = 50$ kPa and $T \sim 300 - 422$ K) CaltechMech performs best at rich conditions ($\Phi = 1.4$); the RMSE for set H is 5.0 cm/s, approximately 24% and 38% smaller than the RMSE obtained with sets F ($\Phi = 0.9$) and G ($\Phi = 1.1$), respectively. For JetSurF, set H also has the

Data	Reference	P (kPa)	T (K)	Φ	N
A	Present study	100	296	0.76 – 1.42	7
B	Davis and Law [12]	100	300	0.85 – 1.70	16
C	Ji et al. [15]	100	353	0.75 – 1.50	10
D	Kelley et al. [14]	100	353	0.75 – 1.70	19
E	Present study	50	296	0.86 – 1.69	12
F	Present study	50	297 – 423	0.9	5
G	Present study	50	296 – 422	1.1	5
H	Present study	50	296 – 422	1.4	5
I	Present study	40 – 100	357	0.9	4
J	Kelley et al. [14]	100 – 1000	353	0.9	4

Table 2: Experimental data sets of laminar burning speed used for the RMSE calculation to evaluate the performance of the chemical kinetic mechanisms used in the present study.

smallest RMSE (1.8 cm/s) when compared to sets F (RMSE = 4.7 cm/s) and G (RMSE = 3.9 cm/s). In regard to the mechanism of Mével, the leaner data set F has the smallest RMSE (7.9 cm/s) when compared to the close to stoichiometric and rich conditions of sets G (RMSE = 13.1 cm/s) and H (RMSE = 14.8 cm/s), respectively. The mean RMSE across the conditions presented in Table 10 is 5.0 cm/s, 2.8 cm/s, and 9.0 cm/s for CaltechMech, JetSurF, and Mével, respectively. Based on a mean RMSE representation of the model performance, JetSurF is the appropriate chemical kinetic mechanism to use when calculating the laminar burning speed of *n*-hexane-air mixtures across a wide range of conditions. The previous statement is made considering the following approach to performing the calculations: a) Soret and Dufour effects were neglected, and b) only mixture-averaged transport properties were considered.

3.2.2. Sensitivity Analysis

A sensitivity analysis was performed with JetSurF to gain further insight into the chemical kinetics of freely propagating *n*-hexane-air flames; the results are shown in Figs. 11 and 12. For all the conditions tested, the most important reaction

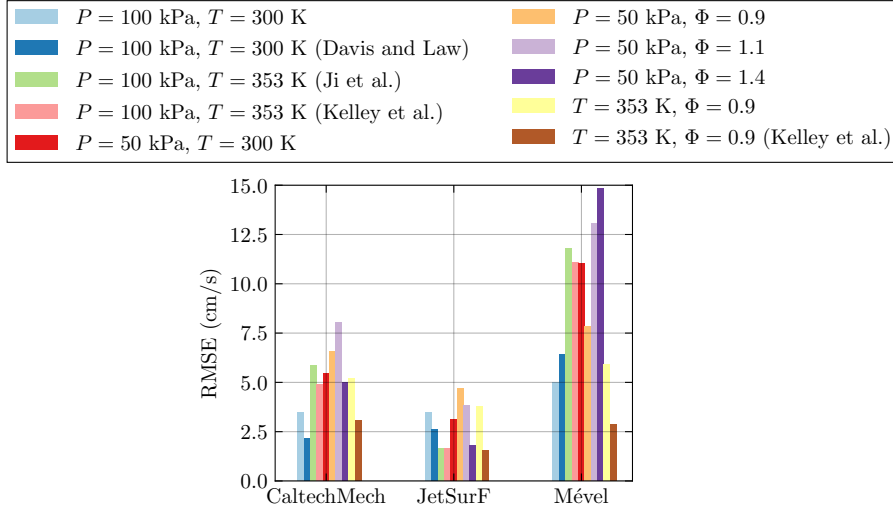


Figure 10: Root-mean-squared-error (RMSE) of the calculated laminar burning speeds using CaltechMech [30], JetSurF [31], and Mével [11].

was the chain-branching reaction R_1 : $\text{H} + \text{O}_2 = \text{OH} + \text{O}$. The sensitivity coefficient of this reaction increases as pressure increases and decreases as temperature increases. The second most sensitive reaction for all conditions tested was R_2 : $\text{p-C}_3\text{H}_4 + \text{H} = \text{A-C}_3\text{H}_4 + \text{H}$ which exhibited a positive coefficient. For the lean mixture ($\Phi = 0.9$), the third most important reaction for all temperatures and pressures investigated was R_3 : $\text{CO} + \text{OH} = \text{CO}_2 + \text{H}$. R_3 is important due to: (1) its high exothermicity which contributes to a temperature increase and speeds up the overall reaction rate, and (2) the generation of the H atom. The fourth most important reaction for the lean mixture was the recombination reaction R_4 : $\text{H} + \text{OH} (+\text{M}) = \text{H}_2\text{O} (+\text{M})$. At low pressure, and for all the temperatures tested, the sensitivity coefficient of R_4 was positive. However, as the pressure increased, the sensitivity coefficient became negative. This is due to the increased competition between the chain branching reaction R_1 and the termination reaction R_4 as pressure increases.

For the rich mixture ($\Phi = 1.4$), as a result of the deficiency of oxygen, reactions R_3 and R_4 do not appear within the most important reactions. The reactions R_5 : $\text{HCO} + \text{H} = \text{CO} + \text{H}_2$ and R_6 : $\text{CH}_3 + \text{H} (+\text{M}) = \text{CH}_4 + \text{H} (+\text{M})$ exhibited negative sensitivity coefficients because they reduce the pool of free radicals by consuming the H atom.

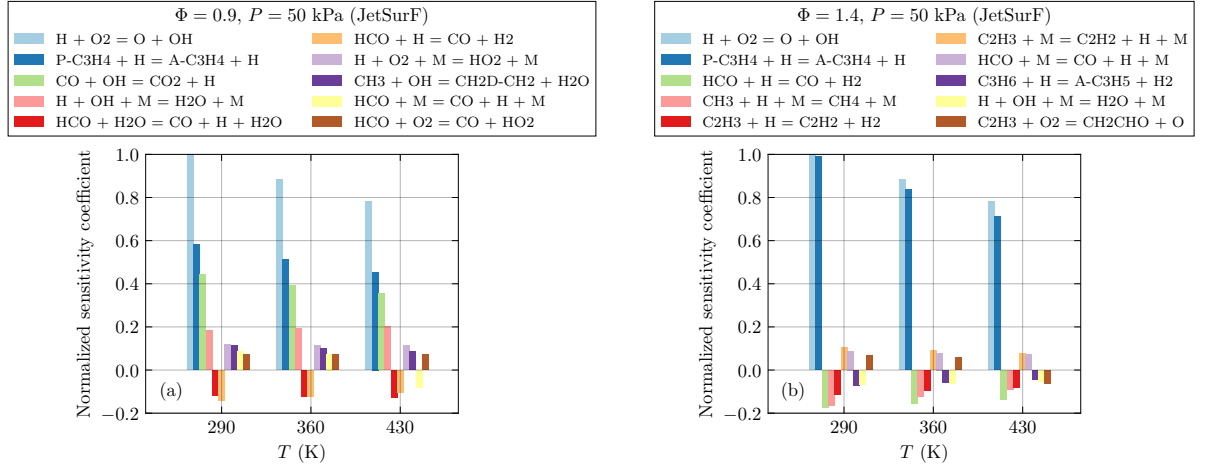


Figure 11: Normalized sensitivity coefficient as a function of initial temperature at an initial pressure of 50 kPa for (a) $\Phi = 0.9$ and (b) $\Phi = 1.4$ using JetSurF [31].

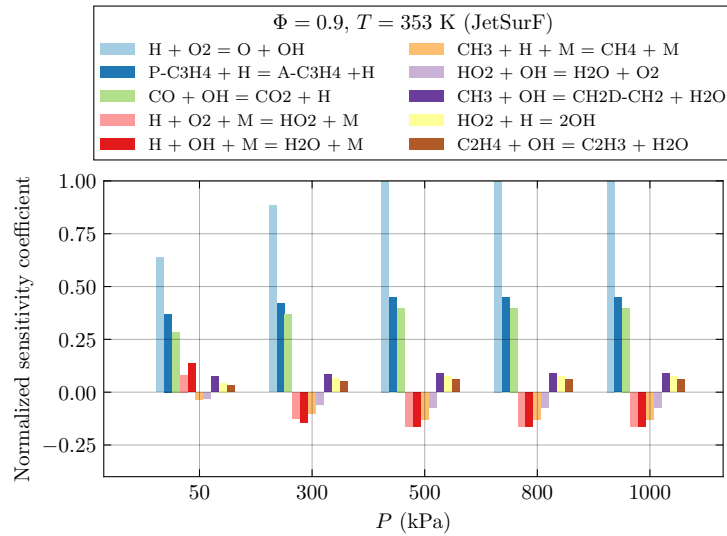


Figure 12: Normalized sensitivity coefficient as a function of initial pressure at an initial temperature of 353 K and $\Phi = 0.9$ using JetSurF [31].

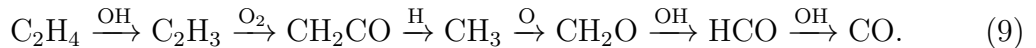
3.2.3. Reactions Pathway Analysis

A reaction pathway analysis was performed using Cantera [39] for a lean n -hexane-air mixture at $\Phi = 0.90$ and initial temperature and initial pressure of 296 K and 50 kPa, respectively, using JetSurF. The reaction pathway was obtained as elementary mass fluxes and was performed with a threshold of 10% in order to focus on the most important pathways. Figure 13 shows a typical example of a reaction

pathway obtained at a distance of 4.9 mm from the flame front and a corresponding temperature of 1443 K. Hexane consumption is mainly driven by H-abstraction reactions, with the OH radical being the most efficient abstracter. The 1-hexyl radical undergoes isomerization which increases the yields of 2-hexyl and 3-hexyl radicals. Conversely, hexane undergoes C-C bond fission leading to ethyl, propyl and butyl radicals. The consumption of 2-hexyl and 3-hexyl radicals also occurs mainly through C-C bond rupture which leads to the formation of a significant amount of C₂H₄. Ethylene consumption eventually leads to CO formation mainly through the following sequences:



and



At the temperature considered, no significant conversion of CO into CO₂ was detected. This reaction pathway analysis underlines the importance of ethylene which appears as a “bottle-neck” species in the course of hexane oxidation.

4. Summary

n-Hexane-air mixtures were characterized through experimental measurements and calculations of the laminar burning speed. The laminar burning speed was obtained by using a nonlinear methodology. The effect of equivalence ratio, temperature, and pressure on the laminar burning speed was investigated experimentally by varying the equivalence ratio $\Phi = 0.62 - 1.60$, the initial temperature from 296 K to 422 K, and the initial pressure from 50 kPa to 100 kPa. The laminar burning speed was observed to increase as pressure decreases ($T = 357$ K) and as temperature increases. It was also shown that the laminar burning speed increases at comparable rates as temperature increases for mixtures at $\Phi = \{0.90, 1.10, 1.40\}$. The predictive capabilities of three chemical kinetic mechanisms from the literature were quantitatively evaluated using the present experimental data and those from the literature. Based on a RMSE analysis, it was shown that JetSurF was the most appropriate

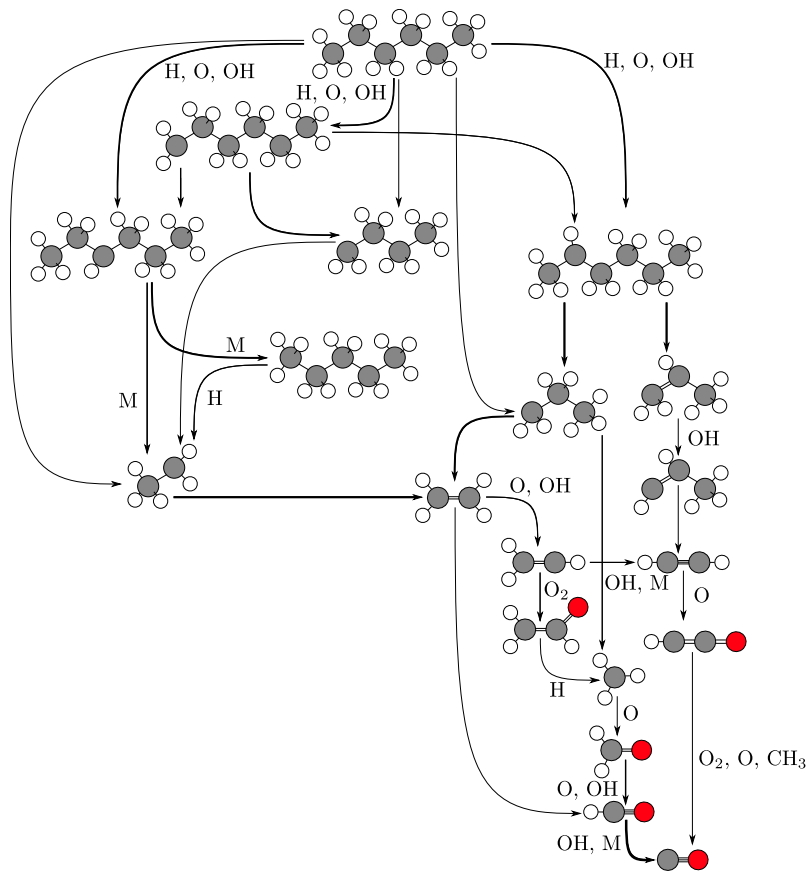


Figure 13: Reaction pathway analysis for the carbon element in a lean n -hexane-air flame at $\Phi = 0.90$ and initial temperature and initial pressure of 296 K and 50 kPa, respectively. Position and temperature in the flame are 4.9 mm and 1443 K, respectively.

mechanism for modeling the laminar burning speed of n -hexane-air mixtures over a wide range of mixture compositions and thermodynamic conditions.

Acknowledgments

This work was carried out in the Explosion Dynamics Laboratory of the California Institute of Technology, and was supported by The Boeing Company through a Strategic Research and Development Relationship Agreement CT-BA-GTA-1.

References

- [1] P. A. Boettcher, R. Mével, V. Thomas, J. E. Shepherd, Fuel 96 (2012) 392–403.

- [2] S. P. M. Bane, Spark Ignition: Experimental and Numerical Investigation With Application to Aviation Safety, Ph.D. thesis, California Institute of Technology, 2010.
- [3] P. A. Boettcher, Thermal Ignition, Ph.D. thesis, California Institute of Technology, 2012.
- [4] S. K. Menon, P. A. Boettcher, B. Ventura, G. Blanquart, *Combustion and Flame* 163 (2016) 42 – 53.
- [5] J. Simmie, *Progress in Energy and Combustion Science* 29 (2003) 599–634.
- [6] H. Curran, P. Gaffuri, W. Pitz, C. Westbrook, W. Leppard, in: SAE International Fuels and Lubricants Meeting and Exposition.
- [7] A. Burcat, E. Olchanski, C. Sokolinski, *Israel Journal of Chemistry* 36 (1996) 313–320.
- [8] V. P. Zhukov, V. A. Sechenov, A. Y. Starikovskii, *Combustion and Flame* 136 (2004) 257–259.
- [9] K. Zhang, C. Banyon, C. Togbé, P. Dagaut, J. Bugler, H. J. Curran, *Combustion and Flame* 162 (2015) 4194 – 4207.
- [10] R. Mével, U. Niedzielska, J. Melguizo-Gavilanes, S. Coronel, J. E. Shepherd, *Combustion Science and Technology* 188 (2016) 2267–2283.
- [11] R. Mével, K. Chatelain, P. A. Boettcher, J. E. Shepherd, *Fuel* 126 (2014) 282–293.
- [12] S. Davis, C. Law, *Combustion Science and Technology* 140 (1998) 427–449.
- [13] J. Farrell, R. Johnston, I. Androulakis, in: SAE Technical Paper, 2004-01-2936.
- [14] A. P. Kelley, A. J. Smallbone, D. L. Zhu, C. K. Law, *Proceedings of the Combustion Institute* 33 (2011) 963–970.
- [15] C. Ji, E. Dames, Y. Wang, H. Wang, F. Egolfopoulos, *Combustion and Flame* 157 (2010) 277–287.

- [16] D. Nativel, M. Pelucchi, A. Frassoldati, A. Comandini, A. Cuoci, E. Ranzi, N. Chaumeix, T. Faravelli, *Combustion and Flame* 166 (2016) 1 – 18.
- [17] R. Mével, F. Lafosse, N. Chaumeix, G. Dupré, C.-E. Paillard, *International Journal of Hydrogen Energy* 34 (2009) 9007–9018.
- [18] P. D. Ronney, G. I. Sivashinsky, *SIAM Journal on Applied Mathematics* 49 (1989) 1029–1046.
- [19] B. Karlovitz, J. Denission, D. Knapschaffer, F. Wells, *Proceedings of the Combustion Institute* 4 (1953) 613–620.
- [20] N. Lamoureux, N. Djebaili-Chaumeix, C. Paillard, *Experimental Thermal and Fluid Science* 27 (2003) 385–393.
- [21] K. Aung, M. Hassan, G. Faeth, *Combustion and Flame* 109 (1997) 1–24.
- [22] D. Dowdy, D. Smith, S. Taylor, A. Williams, *Proceedings of the Combustion Institute* 23 (1990) 325–332.
- [23] S. Jerzembeck, M. Matalon, N. Peters, *Proceedings of the Combustion Institute* 32 (2009) 1125–1132.
- [24] D. Bradley, P. Gaskell, X. Gu, *Combustion and Flame* 104 (1996) 176–198.
- [25] A. N. Lipatnikov, S. S. Shy, W. yi Li, *Combustion and Flame* 162 (2015) 2840 – 2854.
- [26] F. Halter, T. Tahtouh, C. Mounaïm-Rousselle, *Combustion and Flame* 157 (2010) 1825–1832.
- [27] N. Bouvet, C. Chauveau, I. Gökalp, F. Halter, *Proceedings of the Combustion Institute* 33 (2011) 913–920.
- [28] A. Kelley, C. Law, *Combustion and Flame* 156 (2009) 1844–1851.
- [29] H. Pitsch., *Flamemaster*, a C++ computer program for 0D combustion and 1D laminar flame calculations, 1998.

- [30] G. Blanquart, P. Pepiot-Desjardins, H. Pitsch, *Combustion and Flame* 156 (2009) 588–607.
- [31] H. Wang, E. Dames, B. Sirjean, D. A. Sheen, R. Tango, A. Violi, J. Y. W. Lai, F. N. Egolfopoulos, D. F. Davidson, R. K. Hanson, C. T. Bowman, C. K. Law, W. Tsang, N. P. Cernansky, D. L. Miller, R. P. Lindstedt, A high-temperature chemical kinetic model of *n*-alkane (up to *n*-dodecane), cyclohexane, and methyl-, ethyl-, *n*-propyl and *n*-butyl-cyclohexane oxidation at high temperatures, JetSurF version 2.0, <http://web.stanford.edu/group/haiwanglab/JetSurF/JetSurF2.0/index.html>, 2010.
- [32] J. Huo, S. Yang, Z. Ren, D. Zhu, C. K. Law, *Combustion and Flame* 189 (2018) 155–162.
- [33] F. Wu, W. Liang, Z. Chen, Y. Ju, C. K. Law, *Proceedings of the Combustion Institute* 35 (2015) 663–670.
- [34] G. Jomaas, C. Law, J. Bechtold, *Journal of Fluid Mechanics* 583 (2007) 1–26.
- [35] Y. Xin, C.-J. Sung, C. K. Law, *Combustion and Flame* 159 (2012) 2345–2351.
- [36] H. Bongers, L. P. H. D. Goey, *Combustion Science and Technology* 175 (2003) 1915–1928.
- [37] X. You, F. N. Egolfopoulos, H. Wang, *Proceedings of the Combustion Institute* 32 (2009) 403–410.
- [38] A. J. Smallbone, W. Liu, C. K. Law, X. Q. You, H. Wang, *Proceedings of the Combustion Institute* 32 (2009) 1245–1252.
- [39] D. G. Goodwin, H. K. Moffat, R. L. Speth, *Cantera: An object-oriented software toolkit for chemical kinetics, thermodynamics, and transport processes*, <http://www.cantera.org>, 2017. Version 2.3.0.

Appendix A. Statistical Analysis: Mann-Whitney-Wilcoxon (MWW) RankSum Test

The Mann-Whitney-Wilcoxon (MWW) RankSum test was used to determine if the distribution of measurements in set **A** were the same as the results from set **B**, written symbolically as the null hypothesis $H_0 : \mathbf{A} = \mathbf{B}$. The test also detects shifts in the distributions given by sets **A** and **B**, written as the hypothesis $H_1 : \mathbf{A} \neq \mathbf{B}$. The test ranks $n_{\mathbf{A}} + n_{\mathbf{B}}$ observations of the combined distributions, where $n_{\mathbf{A}}$ and $n_{\mathbf{B}}$ correspond to the number of experimental observations in sets **A** and **B**, respectively. Each observation has a rank, where rank 1 and rank $n_{\mathbf{A}} + n_{\mathbf{B}}$ correspond to the smallest and largest values of S_u^0 . In the following example, set **A** and set **B** correspond to Data A and Data B, respectively, from Table 2. The sum of the rank of set **B** is $W = 200$; under the null hypothesis H_0 , the mean and variance of W is,

$$\mu_W = \frac{n_{\mathbf{B}}(N + 1)}{2} = \frac{16(23 + 1)}{2} = 192, \quad (\text{A.1})$$

$$\sigma_W^2 = \frac{n_{\mathbf{A}}n_{\mathbf{B}}(N + 1)}{12} = \frac{7 \cdot 16(23 + 1)}{12} = 224, \quad (\text{A.2})$$

where $N = n_{\mathbf{A}} + n_{\mathbf{B}}$. The observed value of the test statistic is,

$$Z_{\text{obs}} = \frac{W - \mu_W}{\sigma_W} = \frac{200 - 192}{\sqrt{224}} = 0.5 \quad (\text{A.3})$$

The two-tailed p-value (calculated probability), p , at $Z_{\text{obs}} = 0.5$ is,

$$p(0.5) = 2 \left(1 - \int_{-\infty}^{0.5} \frac{1}{\sqrt{2\pi}} e^{-z^2/2} dz \right) = 0.6 \quad (\text{A.4})$$

Since $p > 0.05$ the differences between sets **A** and **B** are not statistically significant.

The MWW RankSum test was used to compare the laminar burning speeds from Data A and Data E, at 100 kPa (set **A**) and 50 kPa (set **B**) respectively. The sum of the rank of set **B** is 123; under the null hypothesis H_0 , the mean and variance of W is 120 and 140, respectively. The calculated Z_{obs} is 0.3 resulting in a p-value of 0.8; since $p > 0.05$, the differences between sets **A** and **B** are not statistically significant.

Appendix B. Present Study Experimental Results

Test	Φ	T_0 (K)	P_0 (K)	L_B (cm)	ΔL_B (cm)	S_u^0 (cm/s)	ΔS_u^0 (cm/s)
0	1.06	296	100	0.042	0.005	36	2
1	0.76	291	100	0.208	0.019	24	1
2	0.83	296	100	0.153	0.015	29	2
3	0.90	296	100	0.117	0.013	33	2
4	0.98	296	100	0.115	0.012	35	2
5	1.26	296	100	0.067	0.007	36	2
6	1.43	297	100	-0.028	0.006	28	2
9	1.30	298	50	0.041	0.006	39	2
18	1.00	296	50	0.143	0.016	38	2
20	0.89	297	50	0.215	0.018	33	2
24	0.85	297	50	0.187	0.017	35	2
26	0.99	295	50	0.181	0.017	35	2
27	1.10	295	50	0.132	0.018	40	2
29	1.20	296	50	0.098	0.012	39	2
30	1.20	296	50	0.099	0.013	39	2
31	1.30	296	50	0.034	0.004	34	2
32	1.40	296	50	-0.070	0.013	28	2
33	1.50	296	50	-0.300	0.042	20	1
34	1.58	297	50	-0.531	0.031	13	1
38	1.00	297	50	0.152	0.017	39	2
39	1.11	297	50	0.123	0.014	40	2
40	0.90	297	50	0.183	0.017	36	2
41	1.34	297	50	0.001	0.005	31	2
42	1.69	297	50	-1.097	0.087	9	1

Table B.1: Results of spherically expanding flame experiments performed at Caltech.

Test	Φ	T_0 (K)	P_0 (K)	L_B (cm)	ΔL_B (cm)	S_u^0 (cm/s)	ΔS_u^0 (cm/s)
43	0.95	297	50	0.154	0.015	35	2
44	0.86	297	50	0.177	0.016	34	2
45	0.92	313	50	0.173	0.018	40	2
46	1.11	312	50	0.113	0.013	43	3
47	1.41	313	50	-0.057	0.009	29	2
48	0.89	314	50	0.184	0.018	38	2
49	0.90	326	50	0.168	0.026	40	2
50	1.10	325	50	0.138	0.015	46	3
51	1.40	325	50	0.002	0.003	33	2
52	0.90	357	50	0.171	0.015	48	3
53	1.10	358	50	0.120	0.014	53	3
54	1.40	358	50	-0.016	0.003	37	2
55	0.90	380	50	0.162	0.016	52	3
56	1.10	380	50	0.117	0.014	58	3
57	1.40	380	50	0.003	0.001	43	3
58	0.90	357	100	0.080	0.010	42	3
59	0.89	357	80	0.106	0.013	42	3
61	0.90	357	40	0.177	0.017	47	3

Table B.2: Results of spherically expanding flame experiments performed at Caltech [continued].

Φ	T_0 (K)	P_0 (K)	S_u^0 (cm/s)	ΔS_u^0 (cm/s)
1.51	424	50	37	2
1.40	422	50	53	3
1.31	422	50	64	4
1.21	423	50	71	4
1.12	423	51	73	4
1.05	423	51	73	4
0.99	423	51	71	4
0.89	423	51	67	4
1.02	425	51	74	4
1.17	425	51	73	4

Table B.3: Results of spherically expanding flame experiments performed at ICARE-CNRS.

Appendix C. Previous Work Experimental Results

Φ	S_u^0 (cm/s)
0.80	27
0.85	31
0.90	35
0.95	37
1.00	39
1.05	40
1.10	40
1.15	40
1.20	38
1.25	36
1.30	33
1.35	29
1.40	26
1.50	18
1.60	14
1.70	12

Table C.1: Results of experimental laminar burning speeds obtained by Davis and Law [12] at a nominal initial temperature and pressure of 300 K and 100 kPa, respectively.

P_0 (kPa)	S_u^0 (cm/s)
100	42
200	37
500	30
1000	25

Table C.2: Results of experimental laminar burning speeds obtained by Kelley et al. [14] at an equivalence ratio and nominal initial temperature of 0.9 and 353 K, respectively.

Φ	S_u^0 (cm/s)
0.55	19
0.60	25
0.70	41
0.80	52
0.90	59
1.00	70
1.10	74
1.20	76
1.30	72

Table C.3: Results of experimental laminar burning speeds obtained by Farrell et al. [13] at a nominal initial temperature and pressure of 450 K and 304 kPa, respectively.

Φ	S_u^0 (cm/s)
0.75	31
0.80	35
0.85	40
0.90	42
0.95	45
1.00	46
1.05	48
1.10	48
1.15	48
1.20	46
1.25	44
1.30	40
1.35	35
1.40	31
1.45	28
1.50	24
1.55	20
1.60	17
1.70	11

Table C.4: Results of experimental laminar burning speeds obtained by Kelley et al. [14] at a nominal initial temperature and pressure of 353 K and 100 kPa, respectively.

Φ	S_u^0 (cm/s)
0.75	37
0.80	40
0.95	48
1.00	50
1.05	50
1.10	49
1.20	45
1.30	38
1.40	27
1.50	19

Table C.5: Results of experimental laminar burning speeds obtained by Ji et al. [15] at a nominal initial temperature and pressure of 353 K and 100 kPa, respectively.